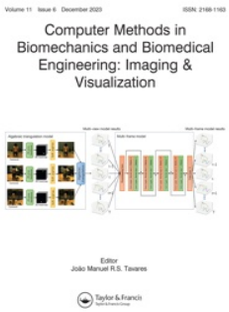

Computer Methods in Biomechanics and Biomedical Engineering: Imaging & Visualization

ISSN: (Print) (Online) Journal homepage: www.tandfonline.com/journals/tciv20

Evaluation of automated airway morphological quantification for assessing fibrosing lung disease

A. Pakzad, WK. Cheung, CHM. Van Moorsel, K. Quan, N. Mogulkoc, BJ. Bartholmai, HW. Van Es, A. Ezircan, F. Van Beek, M. Veltkamp, R. Karwoski, T. Peikert, RD. Clay, F. Foley, C. Braun, R. Savas, C. Sudre, T. Doel, DC. Alexander, P. Wijeratne, D. Hawkes, Y. Hu, JR. Hurst & J. Jacob

To cite this article: A. Pakzad, WK. Cheung, CHM. Van Moorsel, K. Quan, N. Mogulkoc, BJ. Bartholmai, HW. Van Es, A. Ezircan, F. Van Beek, M. Veltkamp, R. Karwoski, T. Peikert, RD. Clay, F. Foley, C. Braun, R. Savas, C. Sudre, T. Doel, DC. Alexander, P. Wijeratne, D. Hawkes, Y. Hu, JR. Hurst & J. Jacob (2024) Evaluation of automated airway morphological quantification for assessing fibrosing lung disease, Computer Methods in Biomechanics and Biomedical Engineering: Imaging & Visualization, 12:1, 2325361, DOI: 10.1080/21681163.2024.2325361

To link to this article: https://doi.org/10.1080/21681163.2024.2325361

Published online: 31 Mar 2024.

COMPUTER METHODS IN BIOMECHANICS AND BIOMEDICAL ENGINEERING: IMAGING & VISUALIZATION
2024, VOL. 12, NO. 1, 2325361
https://doi.org/10.1080/21681163.2024.2325361

Evaluation of automated airway morphological quantification for assessing fibrosing lung disease

A. Pakzad[a,b], WK. Cheung[a,c], CHM. Van Moorsel[d], K. Quan[a,b], N. Mogulkoc[e], BJ. Bartholmai[f], HW. Van Es[g], A. Ezircan[e], F. Van Beek[e], M. Veltkamp[e,h], R. Karwoski[i], T. Peikert[j], RD. Clay[j], F. Foley[j], C. Braun[j], R. Savas[k], C. Sudre[a,l], T. Doel[m], DC. Alexander[a,c], P. Wijeratne[a,c], D. Hawkes[a,b], Y. Hu[a,b], JR. Hurst[n] and J. Jacob[a,n]

[a]Centre for Medical Image Computing, University College London, London, UK; [b]Department of Medical Physics and Biomedical Engineering, University College London, London, UK; [c]Department of Computer Science, University College London, London, UK; [d]Department of Pulmonology, Interstitial Lung Diseases Center of Excellence, St Antonius Hospital, Nieuwegein, the Netherlands; [e]Department of Respiratory Medicine, Ege University Hospital, Izmir, Turkey; [f]Division of Radiology, Mayo Clinic Rochester, Rochester, MN, USA; [g]Department of Radiology, St Antonius Hospital, Nieuwegein, the Netherlands; [h]Division of Heart and Lungs, University Medical Center, Utrecht, the Netherlands; [i]Department of Physiology and Biomedical Engineering, Mayo Clinic Rochester, Rochester, MN, USA; [j]Division of Pulmonary and Critical Care Medicine, Mayo Clinic, Rochester, MN, USA; [k]Department of Radiology, Ege University Faculty of Medicine, Izmir, Turkey; [l]MRC Unit for Lifelong Health & Ageing, University College London, UK; [m]Code Choreography Limited, Bolton, UK; [n]UCL Respiratory, University College London, London, UK

ABSTRACT

Abnormal airway dilatation, termed traction bronchiectasis, is a typical feature of idiopathic pulmonary fibrosis (IPF). Volumetric computed tomography (CT) imaging captures the loss of normal airway tapering in IPF. We postulated that automated quantification of airway abnormalities could provide estimates of IPF disease extent and severity. We propose AirQuant, an automated computational pipeline that takes an airway segmentation and CT image as input and systematically parcellates the airway tree into its lobes and generational branches, deriving airway structural measures from chest CT. Importantly, AirQuant prevents the occurrence of spurious airway branches by thick wave propagation and removes loops in the airway-tree by graph search, overcoming limitations of existing airway skeletonisation algorithms. Tapering between airway segments (intertapering) and airway tortuosity computed by AirQuant were compared between 14 healthy participants and 14 IPF patients. Airway intertapering was significantly reduced in IPF patients, and airway tortuosity was significantly increased when compared to healthy controls. Differences were most marked in the lower lobes, conforming to the typical distribution of IPF-related damage. AirQuant is an open-source pipeline that avoids limitations of existing airway quantification algorithms and has clinical interpretability. Automated airway measurements may have potential as novel imaging biomarkers of IPF severity and disease extent.

ARTICLE HISTORY
Received 18 January 2023
Accepted 24 February 2024

KEYWORDS
Airway morphology; Bronchiectasis; Computed tomography

1. Introduction

We present a clinical tool AirQuant for the comprehensive evaluation of airway structure on volumetric Computed Tomography (CT) imaging of the lungs. We apply AirQuant to quantify traction bronchiectasis in idiopathic pulmonary fibrosis. Taking as input the CT image and a detailed airway segmentation, AirQuant outputs quantitative metrics on each airway segment, indexed by lung lobe and airway generation.

1.1. Bronchiectasis

Airways are tubular branching structures originating centrally from the trachea and extending to the lung periphery. Airways transport gases between the external air and the alveolar sacs at the airway terminus where oxygen exchange into the alveolar capillaries occurs. An airway segment is defined as a continuous tube running between two airway branching points. From the major bronchi that arise from the trachea, each new division of airway branches can be considered a new airway generation. In a healthy individual, airway segments narrow or taper in diameter as they run from the central to the peripheral lung. Tapering occurs both along an airway segment and with respect to the segment of the preceding airway generation Weibel and Gomez (1962).

Bronchiectasis describes a structural airway disease in which the airways lose their healthy tapered structure and become abnormally dilated within a segment. Various lung diseases are associated with bronchiectasis, including those driven by infection and or inflammation in the airway wall. In fibrosing lung diseases, of which idiopathic pulmonary fibrosis (IPF) is the hallmark fibrosing lung disease Hansell et al. (2009) the airways are pulled open by fibrosis and contraction of the surrounding connective tissue and airway dilatation is termed 'traction bronchiectasis'.

Bronchiectasis is typically evaluated by a radiologist following visual inspection of a chest CT scan. Evaluation of the extent and degree of dilatation of bronchiectatic airways allows the characterisation of lung disease severity and extent. In IPF for example, the prognostic importance of airway dilatation has

CONTACT A. Pakzad a.pakzad@cs.ucl.ac.uk Centre for Medical Image Computing, University College London, UK

influenced current diagnostic guidelines. The presence of traction bronchiectasis in an appropriate distribution is now used to classify a CT as demonstrating a probable usual interstitial pneumonia pattern Raghu et al. (2018).

The classical morphological signs of bronchiectasis include a) the visualisation of airways within 1 cm of the lung periphery, b) a lack of tapering of the airway, c) an airway diameter greater than the diameter of the accompanying pulmonary artery Hansell et al. (2008). However, solely relying on the comparison of the airway to its adjacent pulmonary artery can be misleading. Living at high altitude Kim et al. (1997) and normal ageing Matsuoka et al. (2003) can result in non-pathological airway dilation, which can be confused with bronchiectasis. Furthermore, there are pathological mechanisms that can result in changes to the size of the pulmonary artery such as smoking Diaz et al. (2017) and hypoxia-induced pulmonary vasoconstriction as a result of chronic lung disease Dunham-Snary et al. (2017). Typically, the visual markers of bronchiectasis are assessed for severity on an ordinal scale and on a lobar basis Bhalla et al. (1991). However, these scoring systems lack sensitivity, are time consuming to apply and are associated with disagreement between radiologists. Consequently, they are not used in routine clinical practice or research. Moreover, ordinal scores conflate disease extent (number of involved lobar segments) and severity (degree of abnormal airway dilatation) which could potentially dilute the prognostic signal attributable to disease extent or severity individually.

Computational image analysis of lung CT imaging may allow the derivation of objective robust quantitative measures of abnormal airway dilatation extent and severity by quantifying dilatation to the nearest millimetre. The precise quantification of airway damage, may identify IPF patients at risk of rapid disease progression. Identification of such patients would be an important cohort enrichment strategy for recruitment into clinical trials of novel IPF therapies Johannson et al. (2015); Collard et al. (2015).

1.2. Idiopathic pulmonary fibrosis

IPF is a lung disease characterised by excessive fibrosis in the structural framework of the lung. The fibrotic process characteristically causes traction bronchiectasis in the lung periphery. There are 80,000 new cases of IPF diagnosed every year across Europe and the United States Hutchinson et al. (2015) with patients typically surviving only 3–5 years following diagnosis Spencer et al. (2021).

1.3. Previous works

Acquiring tapering measurements involves executing an airway measurement algorithm at a perpendicular plane to the airway centreline at regular intervals, as demonstrated in Figure 1(a). This can be achieved after airway lumen segmentation and centerline extraction. The full width at half maximum edge cued segmentation limited (FWHMESL) technique considers a one-dimensional profile through the airway wall from inside the airway lumen to outside. The airway wall traces a bell-shaped curve. The boundary edges lie at the half-maximum value Kiraly et al. (2005); Odry et al. (2006). Other methods for estimating the airway wall edge exist but require manual parameter tuning Petersen et al. (2014); Weinheimer et al. (2008).

There have been efforts to compare airway metrics derived from an airway tree, such as tapering, both between individuals and between specific disease groups. Quan et al. (2018) considered a solitary individual airway path, defined as a contiguous path through the airway tree from carina to the most distal point in the segmentation. They presented a log-tapering index defined as the slope of fitted arc length to log-area curve along the individual airway. Whilst the study showed that individual bronchiectatic airways and normative airways differed by their log tapering index, the limitation of the methodology was that only a single path in the airway tree was ever considered. Weinheimer et al. (2017) demonstrated YACTA, a graph-based airway tree analysis software. They classified airways by lobe and generation and considered an airway taper index per segment which was compared to the preceding segment. They found moderate correlation with visual scoring in 36 patients with CF assessed at multiple timepoints. They also acknowledged the importance of lobe and lingula segment distinction though they did not detail their adapted lobe classification methodology. The measure of airway (inter)taper index described in the study required an unvalidated assumption on the nature of airway intertapering, namely that it was linear across generations. Kuo et al. (2020) similarly derived the airway tree by a graph-based method. Airways were matched with adjacent arteries, dividing airways into groups based on size of arteries into 'large', 'regular' and 'small' though the method did not localise airways by lobe. Across these three size groupings, measures of intertapering (relative change in average diameter of an airway segment compared to its parent segment), intratapering (change in diameter within airway) were shown to differ in 12 children with bronchiectasis compared to normal scans. Measures were expressed using median values and were therefore agnostic to the underlying distribution of disease. Unfortunately, the study did not demonstrate the extent of airway segmentations achieved by the method. A disadvantage of classifying airways according to the size of the paired pulmonary artery is that this ignores the lobar location of the airway. Many lung diseases are geographically localisedfor example, IPF localises to the base of the lower lobes, whilst cystic fibrosis localises to the upper lobes. This makes lobar localisation of damage a crucial determinant for disease diagnosis and in turn, estimation of disease severity. Furthermore, classifying airways according to the size of the accompanying pulmonary artery assumes that the artery itself is not modified in its size by the presence of disease.

The methodology presented in this manuscript can be applied to a CT after any existing airway tree segmentation algorithm. The presented airway segmentation is based on recent practices and we do not claim the presented method as novel. AirQuant is a graph-based airway tree analysis framework that exists distinct to the airway segmentation process that utilises and expands on methods laid out in Quan et al. (2018).

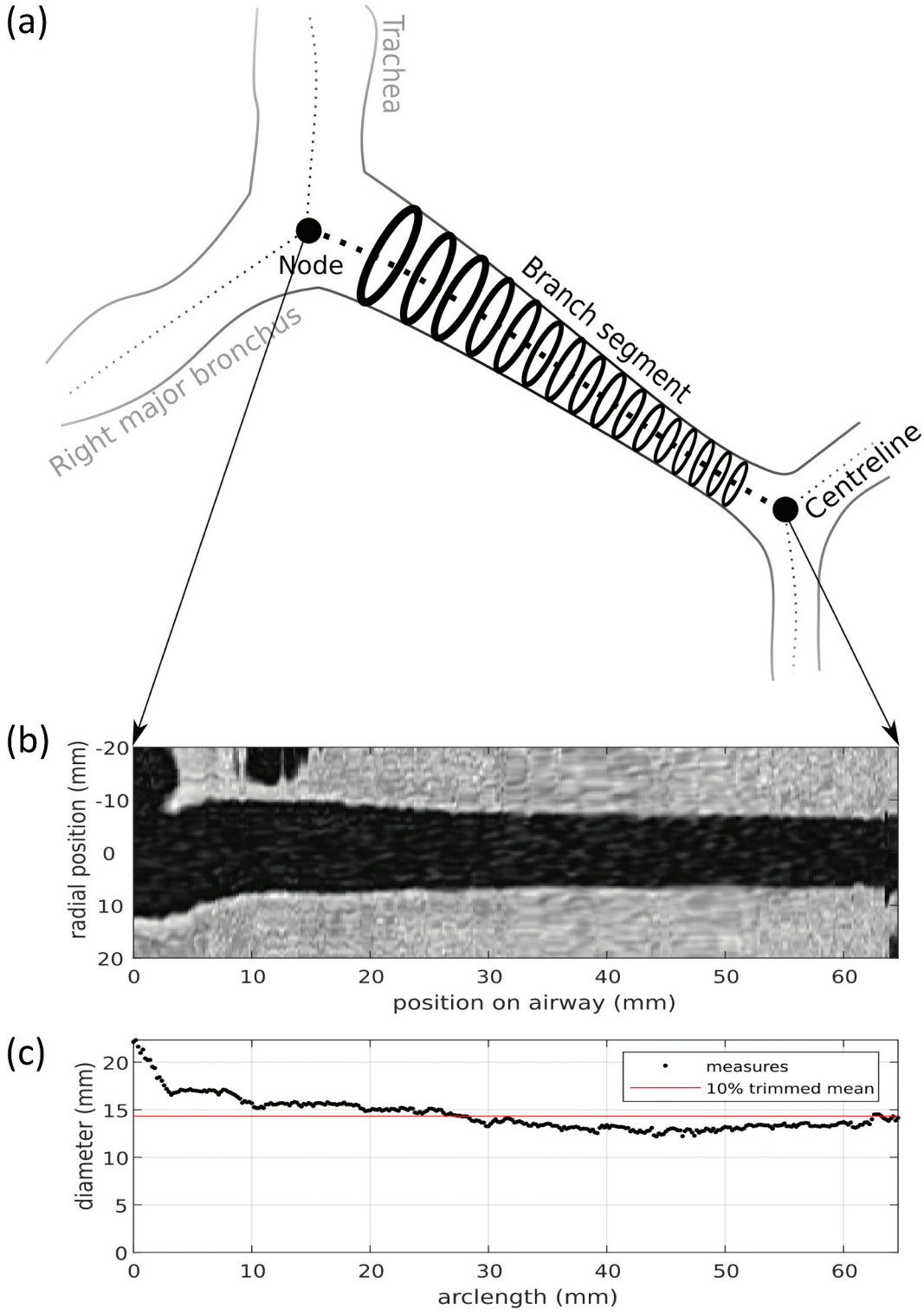

Figure 1. Example of how tapering measures are derived for a given airway. Here the left major bronchus is demonstrated. (a) The airway is outlined with a solid line with its segmentation-derived centreline represented by a dashed line. An airway segment is typically bounded by nodes which represent splitting of airways or end points. The airway diameter is measured at regular intervals between nodes along the segment, shown here as bold rings. (b) Our technique uses the reformatted CT interpolated along the airway segment's centreline between nodes. Diameters corresponding to the airway positions in (b) are measured using the presented pipeline, AirQuant (c). The 10 percent trimmed-mean, i.e. uses the central 90% of diameter measures to derive the mean, highlighted in red.

1.4. Presenting AirQuant

In this paper, we adapt existing skeletonisation methods to reliably extract airway centrelines and branching tree-like structures. To replicate lung lobar classification systems used in standard radiological assessment, we have adapted an automated lobar classification system that delineates the lingula (nominally part of the left upper lobe) as a distinct lobe. We consider inter-branch tapering (intertapering) and airway tortuosity between disease groups. We consider the median of these measures in any airway segment group so as to not make assumptions on an underlying distribution of airway segmentation.

We propose a computational pipeline that takes as input an airway segmentation and CT image and provides an objectively derived end-to-end measure of airway morphology. It requires little to no manual input, making it a feasible clinical tool to measure airways in order to support clinical assessment. A novel graphical abstraction of the airway tree to its fundamental morphology is also presented. Our methodology is released as an open source and documented framework for the development of airway tree analysis.

The lungs are classified by lobe and by airway generation allowing easy localisation of focal airway abnormalities. We describe various quantitative expressions of airway morphological abnormality in IPF patients that delineate the extent and severity of fibrosis-related airway damage. We contrast findings in IPF with airway metrics in healthy volunteers and provide the first quantitative measurement of airway tortuosity which has only previously been qualitatively considered in the context of pulmonary fibrosis Westcott and Cole (1986).

2. Methods

Following automated airway segmentation based on a trained dilated 2D-UNet combined with region-growing, the proposed AirQuant pipeline to process a chest CT is shown in Figure 2. The centreline is first extracted by thinning (Figure 2(a)) and a network graph is derived. The airway tree is parcellated into its individual branching segments where graph edges and splitting/end points are represented by nodes. (Figure 2(b)). Cubic splines are then fitted to each segment's associated centreline points, allowing sub-voxel interpolation along the airway segment ((Figure 2(c)). By taking the tangent to the spline at intervals, CT patches in the plane perpendicular to the airway centreline can be cubically interpolated (Figure 2(d)). From these patches, the airway luminal diameter is measured using the (FWHMESL) technique by Kiraly et al. (2005), implemented by Quan et al. (2018), which has been further refined to improve robustness of airway measurement (Figure 2(e)). Using the set of luminal diameter measurements and total arc-length by spline fitting, metrics can be derived that describe each individual airway segment.

All code was written and executed in MATLAB, available at https://github.com/ashkanpakzad/airquant.

2.1. Study data

We consider 14 healthy never-smokers (from Mayo Clinic, Rochester, Minnesota, USA) and 14 IPF patients with varying levels of disease severity from two centres (11 from St Antonius Hospital, Utrecht, the Netherlands and 3 from Ege University Hospital, Izmir, Turkey). Lung function measures obtained included forced vital capacity (FVC) in all subjects and diffusing capacity of the lungs for carbon monoxide (DLCO) in the IPF group alone. Lung function measurements were obtained within 90 days of CT scan acquisition. Visual CT scores of interstitial lung disease (ILD) extent and traction bronchiectasis was performed on IPF scans by an experienced radiologist (Joseph Jacob). Further details of the study data are included in Table 1. None of the cases analysed in this study were used to train or test the airway segmentation algorithm mentioned in section 2.2.1.

Approval for this retrospective study of pulmonary function and CT data was obtained from the local research ethics committees and Leeds East Research Ethics Committee: 20/YH/0120. The requirement for informed consent was waived by local research ethics committees for the IPF patients. The study of healthy volunteers was approved by the Mayo Clinic Institutional Review Board and informed consent was obtained from all study participants.

2.2. Automated airway segmentation

As an airway segmentation is required to measure airway tapering, we implement an ensemble method using a trained 2D

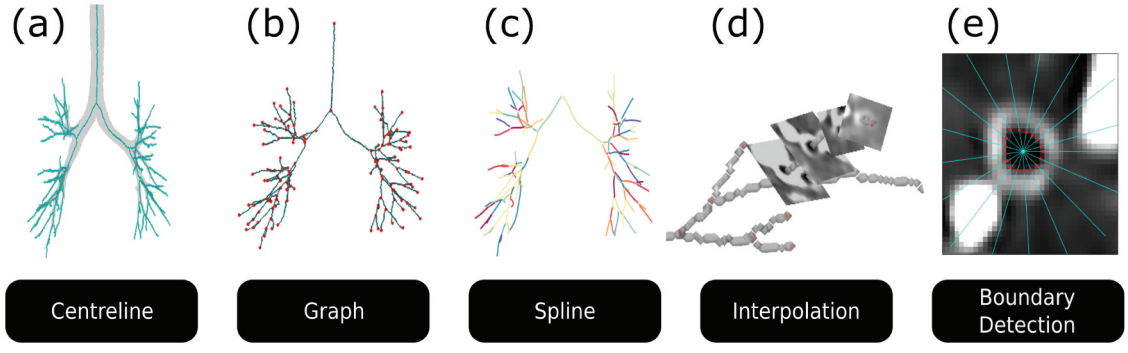

Figure 2. Demonstrating the AirQuant pipeline graphically from left to right for a given airway lumen segmentation through to the end where the lumen boundary is established.

Table 1. Technical details of the CT data used in this study. Values shown as median (inter quartile range) across cases where applicable. Age, FVC and number of lobe segments were compared by mann-whitney U test. Sex was compared by chi-squared test. Significance of each comparison shown * $p < 0.05$, * $p < 0.01$, *** $p < 0.001$ and **** $p < 0.0001$. We denote the left lingula segments as the left middle lobe. IPF = idiopathic pulmonary fibrosis; ILD = interstitial lung disease; FVC = forced vital capacity; DLCo = diffusing capacity of the lungs for carbon monoxide.

Feature	Normal	IPF
Number of cases	14	14
Age (years)**	45.50 (33.50–54.50)	59.0 (57.35–69.00)
Sex (male/female)*	7/7	13/1
FVC (%)****	103.83 (99.68–107.89)	75.34 (64.57–85.12)
DLCo (%)		47.63 (41.56–55.59)
Mean ILD extent	0.00 (0.00–0.00)	24.58 (19.06–30.00)
Traction bronchiectasis score		
Right upper lobe	0.00 (0.00–0.00)	2.50 (2.00–3.00)
Left upper lobe	0.00 (0.00–0.00)	1.50 (1.30–2.00)
Right middle lobe	0.00 (0.00–0.00)	2.00 (2.00–2.00)
Left middle lobe	0.00 (0.00–0.00)	2.00 (1.63–2.00)
Right lower lobe	0.00 (0.00–0.00)	3.00 (2.50–3.00)
Left lower lobe	0.00 (0.00–0.00)	3.00 (2.25–3.00)
Slice pixel size (mm)	0.74 (0.70–0.74)	0.72 (0.68–0.73)
Slice thickness (mm)	1.00 (1.00–1.00)	0.75 (0.70–0.80)
Reconstruction diameter (mm)		371 (357–279)
Reconstruction kernels	Bv49d	C, YC, BONE, EC, YB, L, STANDARD, B18f
Manufacturer		Philips, Siemens, GE Medical Systems
Peak voltage (kV)		120 (120–120)
X-ray current (mA)		200 (154–301)
Total airway segments	128.50 (117.50–148.75)	160.50 (139.50–191.25)
Right upper lobe	28.00 (26.25–30.00)	31.00 (27.25–38.50)
Left upper lobe	20.00 (17.00–21.75)	21.50 (13.00–25.00)
Right middle lobe***	9.50 (7.00–11.75)	15.50 (13.00–24.00)
Left middle lobe	7.00 (5.00–8.00)	7.50 (7.00–12.00)
Right lower lobe*	34.50 (30.25–38.00)	47.50 (42.50–53.00)
Left lower lobe	32.00 (24.00–42.00)	40.50 (31.75–47.50)

dilated UNet model Yu and Koltun (2016) combined with a *region growing algorithm with explosion control* using the software tool, Pulmonary ToolKit (PTK) Doel (2014) .[1] The two methods are executed on each case in parallel, with the results combined by logical union operation. A filter is then applied to only keep the largest 26 voxel connected binary object, resulting in a fully connected main airway tree. Where the deep learning-based segmentation algorithm identifies more peripheral branches, the PTK-based region growing segmentation identifies the trachea and larger branches well for a contiguous airway tree from the trachea towards the bronchioles. The combination of data-driven and rule-based algorithms are intended to maximise segmentation performance.

2.2.1. 2D UNet segmentation

The dilated U-Net model is an improved version of the original U-Net model that replaces standard convolution layers with dilated convolution layers Yu and Koltun (2016). The addition of dilated convolution layers allows the performance of local convolutional operations on a larger region without any increased computational cost but importantly maintains image resolution. Using this methodology provides greater pixel-wise context during training and at inference. Our model was trained on manually segmented airway trees performed in-house under the supervision of an experienced chest radiologist (J. Jacob). The training and validation/testing dataset used in the development of the dilated UNet model comprised six normal CTs in healthy never-smoker volunteers, two normal cases from the EXACT09 competition data set Lo et al. (2012) and 17 IPF cases, totalling 25 volumetric CTs. The images used in these datasets were mutually exclusive. The axial slices of all CTs were amalgamated, randomised and split 80–20 into training and validation datasets, respectively. None of the images used to train/validate/test the dilated U-NET model were analysed in the current clinical study. As a 2D input model, the dilated U-NET only considered one axial CT slice at a time, without the context of the rest of the CT volume. Training was implemented using Adam optimiser Kingma and Ba (2014), minimising the combined binary cross entropy Goodfellow et al. (2016) and dice similarity coefficient loss functions Dice (1945). The learning rate was initially set to 1e-5, reducing to 1e-6 upon loss plateau over three consecutive training epochs. The model achieved a training and validation dice score of 88.5% and 87.2%, respectively. Implementation was in Tensorflow Martín et al. (2015) and Keras Chollet et al. (2015) with Python.

The data were preprocessed by limiting intensity levels to a standard lung window, level −500 Hounsfield Units (HU) and width 1500 HU, and then normalising to a range from 0 to 1. The slice size was limited to 512×512 pixels. Larger raw CT slices were downsampled by cubic interpolation to pass through the fixed-size model and inferred labels upsampled to the original size by nearest-neighbour interpolation. All analyses were conducted on the original image size. At inference, we input each axial slice from a single CT case into the model, and combine the individual slice results to generate a 3D segmentation result.

2.2.2. Pulmonary toolkit segmentation

The Pulmonary Toolkit (PTK) Burrowes et al. (2017) implements airway segmentation by region growing from a tracheal seed.

The algorithm starts by thresholding the CT to air voxel density (less than −775 HU). It then identifies the trachea in the upper superior section of the CT as the largest connected component of air voxels and chooses pixels towards the top of the structure to form the tracheal seed. A wave-front propagates from the tracheal seed and travels through the thresholded air mask, classifying the volume traversed as part of the airway tree. Complete splitting of a wave-front indicates new airway branches, with the resultant wave-fronts becoming independent of each other. Wave-fronts maintain a thickness of multiple voxels in larger airways, which prevents splittings that would likely result in spurious branches due to CT partial volume artefact. Sudden increases in volume of wave growth indicate parenchymal leakage of the wave-front. Leakage is controlled by an *explosion multiplier*, set such that if the number of new voxels in a wave front are more than the factor of the explosion multiplier of the previous wavefront. The wave-front defaults to its previous iteration and grows no-more. The default PTK settings used to avoid parenchymal leakage were implemented i.e. explosion multiplier was set to 7 and wave-fronts were not allowed to grow beyond 15 generations.

2.3. Centreline extraction

PTK's full skeletonisation method Doel (2012) is used here on the final airway segmentation. This is a thinning algorithm based on Palágyi et al. (2006). It first identifies airway endpoints by re-running the same wave propagation step as the airway segmentation algorithm described above 2.2.2, without explosion control or generational limit. The thick wave-propagating component helps to delineate false airway branches from real branches, thereby identifying true airway endpoints. The trachea is marked as an airway endpoint from the outset. The binary object bounded by all endpoints is then iteratively reduced to its topological centreline. Although false branches are robustly removed, airway loops may have occurred at this stage, as topological thinning does not reflect the true anatomical tree structure of the airways.

A key innovation of PTK's skeletonisation method is a post-processing step which removes inner loops by retracing out the whole skeleton voxel-by-voxel, parsing branch segments in a depth-first-search style. Starting from the top of the trachea, it considers the 27-connected neighbour skeleton voxels of the last traced voxel to determine which voxel should be added to grow the airway segment. Upon reaching the end of a segment, i.e. a bifurcation point, it has fully parsed the current segment and starts parsing one of two (or more) new child-branches. In doing so, it acknowledges the discovery, though does not immediately parse that child-branch's sibling(s). It holds in memory the first voxel of every new segment it discovers. If a candidate skeleton voxel is found to match the first voxel of a discovered non-parsed segment, then it identifies that the whole candidate segment forms a loop. The offending segment is then terminated and removed from the final skeleton.

2.4. Airway parcellation

To facilitate analysis, the airway tree is divided into airway segments. This definition enables direct conversion of the airway centreline into a graphical network representation Kollmannsberger et al. (2017), where graph edges become airway segments and airway division points or airway endpoints become graph nodes (Figure 2(b)). The graph is converted into a digraph (directional graph), edges are orientated to direct away from the highest point node, the top of the trachea. As a digraph, the carina (point of division of the main bronchi from the trachea) can be identified as the node with the greatest outcloseness graph centrality metric. It is the closest node to reach all nodes in both the left and right lungs. This digraph orientation means that airway segments are point from the central lungs outwards. Setting a direction in the graph facilitates subsequent steps in the pipeline, dictates the direction in which the spline is sampled and supports airway generation classification and lung lobe classification. Each individual airway segment has a cubic spline (piecewise polynomial function) fitted to its collective centreline points which is smoothed by a moving average along the segment starting from the proximal segment and moving distally. The spline is sampled at equidistant intervals, tracking the tangent of the spline at these points to calculate the airway's perpendicular plane for diameter measurements. The limit of resolution for the change in airway diameter is considered to be no less than half the shortest voxel diameter. All interpolation sampling sizes are set individually for each given CT image at half the shortest voxel diameter.

2.5. Airway measurement

The CT image is interpolated at spline sample points perpendicular to the tangent of the spline such that the resultant image produces a slice along the natural long axis of the airway (Figure 2(d)). The interpolation pixel size is dynamically set to half the shortest voxel diameter of the given CT. Diameter measurements are made on these airway-perpendicular slices at spline sampling intervals.

On the airway-perpendicular slices, several radial density profiles that are uniformly spaced originate from the lumen centre, sampling the change in HU; a technique known as *raycasting*. These radial profiles of the airway wall typically appear as a Gaussian curve, due to the nature of CT imaging of thin structures Weinheimer et al. (2008). It is approximated that the wall centre falls at the Gaussian maximum and that the inner and outer boundary fall at the FWHM points, i.e. the half-intensity points either side of the curve. However, due to the nature of CT imaging and proximity of lung vessels to the airways, the radial profile does not always appear as a smooth Gaussian. In reality, these HU density profiles can appear noisy with several maxima. The airway segmentation is also interpolated at the same points as the CT. The nearest local maxima to the boundary of the airway segmentation is considered the wall peak. This method is known as the FWHMESL technique as described by Kiraly et al. (2005), and implemented and validated by Quan et al. (2018) on phantoms down to 2.5*mm*. The inner airway lumen boundary is therefore identified as the first half-maximum. The second half-maximum relating to the outer wall boundary is often found to be more susceptible to noise, as the outer airway wall may have a structure with similar

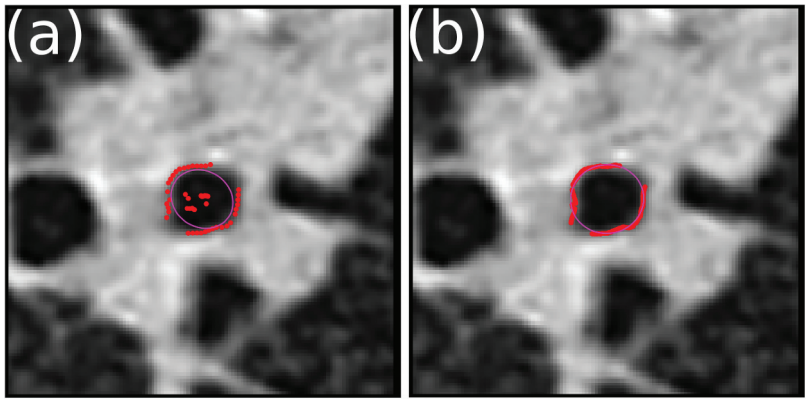

Figure 3. Airway measurement slices of the same perpendicular airway slice. Dots represent inner airway boundary detection of each raycast point. The ellipse is fitted to these points to derive final diameter measurements. (a) original method by Quan et al. (2018) and (b) with our increased number of ray points and addition of outlier removal mechanism. Note that in (a) the ellipse is poorly fitted to the boundary due to raycast points that prematurely stop due to image noise. In (b) these false boundary points are classified as outliers and are therefore removed before fitting the ellipse.

contrast and density obscuring its boundary, e.g. a blood vessel. Thus we only consider the accurately determined inner boundary (Figure 2(e)).

As a perpendicular section through the long axis of an airway forms an ellipse, an ellipse is fitted Fitzgibbon et al. (1996) to the inner wall boundary points. The ellipse total area, A_E is calculated and a generalised diameter D_G derived for that point in the airway segment.

$$D_G = 2\sqrt{\frac{A_E}{\pi}}$$

Where our methodology differs from Quan et al. (2018) is that we employ an outlier detection mechanism improving robustness of airway boundary delineation, demonstrated in Figure 3. The distance of each inner lumen point to the centre point is calculated. If this spans greater or less than 3 times the Mean Absolute Deviation (MAD) compared to all other points then it is considered an outlier. To support this, we choose to increase the number of raycast radial density profiles from 50 (every 7.2 degrees of rotation) to 180 (every 2 degrees of rotation). The greater the number of raycasts, the more robust outlier detection becomes, particularly for larger airways where the distance between lumen boundary points will be larger for a given number of raycasts.

Ultimately, an accurate intertapering value relies on accurate average measurements of the current and parent airway segment. By sampling the airway diameter at less than half the smallest CT voxel dimension for each case, we ensure that we get the most accurate diameter measurements these methods can obtain from the CT image. Figure 1(b,c) demonstrates a series of diameter measurements on a single airway segment.

2.6. Phantom study

The same phantom created and considered in Quan et al. (2018) has been used here to evaluate the accuracy of the measurement method described above. Hollow 3D printed tubes were designed to mimic the airways which are surrounded by rice mimicking the lung parenchyma. Four straight 50 mm long tubes with fixed diameters of 2.12, 3.52, 4.92 and 6.32 mm are considered. A similar set of curved phantom airways, with radius of curvatures of 10, 15, 20, 25 and 30 mm each with a fixed diameter of 2.12 mm are also considered.

The phantom underwent CT scanning and was reconstructed using a lung kernel. The in-plane voxel size was 0.625×0.625 *mm* and axial size 1.00 *mm*. The straight tubes were roughly parallel to the axial direction of the scan. The spline and interpolation patch size was therefore 0.3 mm. The ground truth measures of the phantoms were made on higher resolution micro-CT scans.

2.7. Airway lobe classification

Airway lobe classification is based on the method described and evaluated against expert annotations on 300 COPD patients by Gu et al. (2012). The classification algorithm takes the graphical representation of the airway tree described in section 2.4. Out-edges (airway segments themselves) of classified nodes inherit their classification immediately. As described in algorithm 1, it considers the positional coordinates of nodes (see Figure 4) starting from the carina node to identify the main left and right bronchi as well as the left upper (LUL) and lower lobes (LLL). The lingula lobe (left middle lobe (LML)) was identified as the lower branch in the left upper lobe thereby mimicking the lobar classification used in clinical radiological lung assessment. The addition of the LML lobe is our chief adaptation, the remainder of the proposed algorithm follows Gu et al. (2012).

The right upper lobe (RUL) is the first division of the right main bronchus. The processing with which to classify the right middle lobe (RML) and right lower lobe (RLL) is described in algorithm 2. The remaining non-classified right lung is taken as a subset of the overall airway graph and the difference in axial to lateral position of every end node is calculated. The most extreme nodes are considered to originate from the RML and the least extreme from the RLL. Tracing back the paths of these two nodes to the carina identifies the set of branches belonging to the RML. Finally the remaining unclassified airways are assigned to the RLL.

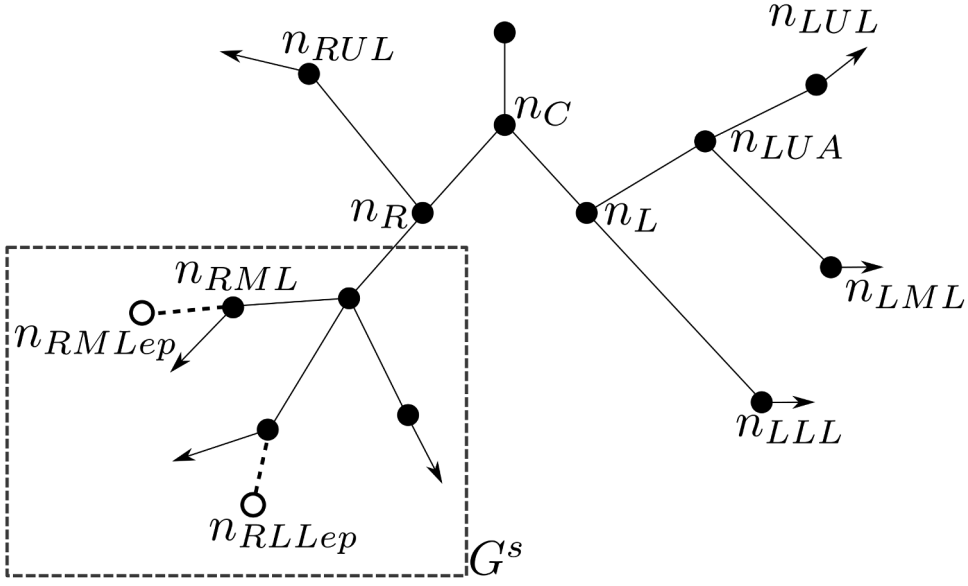

Figure 4. Schematic showing typical airway lobe structure used to automatically classify airways into their lobes. Key airway-tree nodes that are identified in the automated lobe classification algorithm are labelled. The airways arising after a given lobe node are classified into that lobe. Hollow nodes are end-points at the extreme of the airway-tree. Solid lines indicate two nodes that are connected by one airway segment. Dashed lines indicate multiple airway segments between two given nodes. Arrows indicate airways that extend beyond the boundaries of the schematic. G^s represents the airways considered in algorithm 2 to identify the right middle and right lower lobes. n_C, carina node; n_R, right lung node; n_{RML}, right middle lobe node; n_{RMLep}, right middle lobe end point; n_{RLLep}, right lower lobe end point; n_L, left lung node; n_{LUA}, left upper area node; n_{LUL}, left upper lobe node; n_{LML}, left middle lobe node; n_{LLL}, left lower lobe node.

We suggest a quality control check where the reclassification of airways to specific lobes may be required because of anatomical variations of the airways tree. For example the presence of a tracheal bronchus, the most common airway tree variant with a prevalence of 1 percent in the general population Dave et al. (2014) would result in a simple manual reclassification of the right upper lobe bronchi. Since only the final analysis is dependent on the lobe classification, reclassification can be done at the end with no consequence to the pipeline. We implemented high-level functions that allow easy reclassification by indicating the most central airway segment or node for a given lobe.

Algorithm 1 Lobe classification for airways adapted from Gu et al. (2012). For upper, middle and lower left lobe and right upper lobe.

Given directed graph of airways, $G(N, A)$ with N nodes and A edges, $n \in N$ and $e \in A$. Arranged in tree like structure from the carina node n_C. N has positional information associated (x,y,z) in ascending order towards (left, posterior, superior) orientation respectively.

$[n_1, n_2] = E_o(n_C)$ ▷out-edges of carina node
if $n_1(x) > n_2(x)$ **then**
  $n_L \leftarrow n_1$ ▷right lung node
  $n_R \leftarrow n_2$ ▷left lung node
else if $n_2(x) > n_1(x)$ **then**
  $n_L \leftarrow n_2$
  $n_R \leftarrow n_1$
end if
$[n_3, n_4] = E_o(n_L)$
if $n_3(z) > n_4(z)$ **then**
  $n_{LUA} \leftarrow n_3$ ▷Left upper area node
  $n_{LLL} \leftarrow n_4$ ▷Left lower lobe node
else if $n_4(z) > n_3(z)$ **then**
  $n_{UAL} \leftarrow n_4$
  $n_{LLL} \leftarrow n_3$
end if
$[n_5, n_6] = E_o(n_{UAL})$
if $n_5(z) > n_6(z)$ **then**
  $n_{LUL} \leftarrow n_5$ ▷Left upper lobe node
  $n_{LML} \leftarrow n_6$ ▷Left middle lobe node
else if $n_4(z) > n_3(z)$ **then**
  $n_{LUL} \leftarrow n_6$
  $n_{LML} \leftarrow n_5$
end if
▷Left lung now fully classified into lobes
$[n_7, n_8] = E_o(n_R)$
if $n_7(z) > n_8(z)$ **then**
  $n_{RUL} \leftarrow n_7$ ▷Right upper lobe node
else if $n_4(z) > n_3(z)$ **then**
  $n_{RUL} \leftarrow n_8$
end if

Algorithm 2 Lobe classification for airways from Gu et al. (2012) for the right middle and lower lobes.

Given that upper, middle and lower left lobe and right upper lobe nodes have been classified make subgraph of remaining nodes, $G^s(N^s, A^s)$ with N^s nodes and A^s edges, $m \in N^s$ and $e \in b_s$. edges have weight of 1. Carina node, n_C is known. Endpoint nodes are nodes with no out edges, m^{ep}.

$V_{z-y} = [m^{ep}(z)] - [m^{ep}(y)]$ ▷Compute based on position.
$m^{ep}_{RML} \leftarrow argmax(V_{z-y})$ ▷Assigns node based on maximum value index.
$m^{ep}_{RLL} \leftarrow argmin(V_{z-y})$ ▷Assigns node based on minimum value index.
$n^{ep}_{RML} \leftarrow m^{ep}_{RML}$ ▷Assigns same index in G from subgraph.
$n^{ep}_{RLL} \leftarrow m^{ep}_{RLL}$
$p_{RML} \leftarrow shortestpath(G, n_C, n^{ep}_{RML})$ ▷find shortest path through G.
$p_{RLL} \leftarrow shortestpath(G, n_C, n^{ep}_{RLL})$
$p_{RML} \leftarrow reverse(p_{RML})$ ▷reverse order of shortest path.
$p_{RLL} \leftarrow reverse(p_{RLL})$
$V_I \leftarrow intersect((p_{RML}), (p_{RLL}))$ ▷get index of first intersect.
$n_{RML} \leftarrow p_{RML}[V_I - 1]$ ▷node before intersect is first node of RML.
$n_{RLL} \leftarrow n_{unclassified}$ ▷RLL assigned to remaining unclassified nodes.

2.8. Metrics

The two key airway-based metrics that have been computed from the derived data using the analytic pipeline are the airway

inter-tapering gradient and airway tortuosity. Intertapering (Equation 1) describes the difference in average diameter, $\bar{d}$ of an airway to its parent airway $\bar{d}_p$, divided by the average diameter of the parent airway.

$$intertapering = \frac{\bar{d}_p - \bar{d}}{\bar{d}_p} \quad (1)$$

Where average diameter $\bar{d}_p$ is derived from the consecutive diameter measurements from the airway segment described in section 2.5.

Airway tortuosity (Equation 2) describes the arc-length of an airway segment, L_a expressed as a ratio of its euclidean segmental length, L_e.

$$tortuosity = \frac{L_a}{L_e} \quad (2)$$

Where euclidean segmental length L_e is derived from taking the euclidean (straight line) distance between the start and end nodes of the airway segment. Both measures are dimensionless.

2.8.1. Normal generational range

This first evaluation aims to disentangle disease severity and disease extent, to just focus on disease severity. This was done by initially considering the frequency of all airways generations within each lobe in the group of healthy subjects. The range of airway segments in the 25th-75th percentile range were retained. The aim was to exclude the most extreme generations of airways from the analysis and quantify the amount of damage seen in the most frequently segmented airway generations. Henceforth, this 50% airway generational range is referred to as the 'normal generation range'. For each lobe, the normal generation range was found to be RUL: 4–6; LUL: 4–5; RML: 3–5; LML: 3–5, RLL: 4–7, LLL: 4–6.

The airways conforming to the normal generation range were evaluated in IPF patients and healthy volunteers in two

Table 2. Intertapering of every investigated airway within the normal generation range.

	Normal			Idiopathic pulmonary fibrosis			
Lobe	n	Median	IQR	n	Median	IQR	p-value
RUL	323	35.66	15.09	336	32.53	16.59	0.00007
LUL	165	36.89	21.20	160	32.76	18.19	0.00372
RML	111	37.28	16.84	155	28.95	19.07	<0.00001
LML	84	39.75	17.13	99	32.23	15.94	0.00039
RLL	374	37.09	21.09	412	30.00	20.57	<0.00001
LLL	308	40.38	20.26	276	31.81	21.19	<0.00001

Table 3. Tortuosity of every investigated airway within the normal generation range.

	Normal			Idiopathic pulmonary fibrosis			
Lobe	n	Median	IQR	n	Median	IQR	p-value
RUL	323	1.03	0.02	336	1.03	0.03	0.00124
LUL	165	1.02	0.02	160	1.03	0.03	0.00131
RML	111	1.03	0.02	155	1.03	0.02	0.03380
LML	84	1.03	0.02	99	1.03	0.03	0.02630
RLL	374	1.03	0.02	412	1.03	0.03	<0.00001
LLL	308	1.03	0.02	276	1.03	0.03	<0.00001

Table 4. Median lobar intertapering per case within the normal generation range.

	Normal			Idiopathic pulmonary fibrosis			
Lobe	n	Median	IQR	n	Median	IQR	p-value
RUL	14	36.58	4.34	14	32.74	7.23	0.05560
LUL	14	37.79	7.23	14	34.23	6.34	0.16400
RML	14	37.19	7.93	14	30.03	7.30	0.00416
LML	14	40.26	5.24	14	33.34	8.67	0.00027
RLL	14	38.17	3.97	14	29.94	4.93	0.00208
LLL	14	39.94	5.19	14	32.08	8.26	0.00021

Table 5. Median lobar tortuosity per case within the normal generation range.

	Normal			Idiopathic pulmonary fibrosis			
Lobe	n	Median	IQR	n	Median	IQR	p-value
RUL	14	1.029	0.005	14	1.031	0.006	0.19400
LUL	14	1.024	0.007	14	1.031	0.009	0.00173
RML	14	1.025	0.010	14	1.031	0.007	0.21000
LML	14	1.026	0.010	14	1.036	0.015	0.03500
RLL	14	1.027	0.002	14	1.032	0.008	0.00173
LLL	14	1.027	0.005	14	1.033	0.004	0.00143

ways: namely at the airway level and then the patient level. For the airway-level analysis, all individual lobar airways within the normal generation range were compared between IPF patients and healthy volunteers for both the airway intertapering gradient (Table 2) and airway tortuosity (Table 3). For the patient-level analysis, the median lobar inter-tapering gradient (Table 4) and airway tortuosity values (Table 5) were calculated at an individual patient level and compared between IPF patients and healthy volunteers.

2.8.2. Central and peripheral ranges

Two final analyses compared airways at the patient level, but categorised the airways according to their generational level. The first analysis compared the median lobar airway intertapering gradient (Table 6) and airway tortuosity (Table 7) for airway generations 2–6. Airways of generation 2–6 can be segmented by most modern lung airway segmentation algorithms making the results of our airway analyses relatively independent of the quality of a specific segmentation tool. The second analysis eschewed the normal generation range and compared at a patient level the median lobar airway inter-tapering gradient (Table 8) and airway tortuosity values (Table 9) for airway generations 7 and beyond.

2.9. Statistical analysis

Airway values for healthy volunteers and IPF patients are compared using the non-parametric Mann-Whitney U test. The median values for the various airway metrics are compared across equivalent lobes and airway generational ranges between the two study groups.

As this is a pilot study of 28 individuals, multiple comparison corrections are not considered in the main text. These results, which do not alter any conclusions in the paper are shown in the supplementary material.

3. Results

Following successful segmentation, AirQuant analyses were fully executed on all airway segments identified. Figure 5 shows the mean extent of airway segmentations for each study group. The median (25th–75th percentile) number of airways identified in normal and IPF groups was 128.50 (117.50–148.75) and 160.5

Table 6. Median lobar intertapering per case within generations 2–6.

	Normal			Idiopathic pulmonary fibrosis			
Lobe	n	Median	IQR	n	Median	IQR	p-value
RUL	14	38.11	3.50	14	33.66	6.41	0.02120
LUL	14	34.80	6.08	14	31.86	2.32	0.04440
RML	14	37.75	6.32	14	31.88	7.97	0.02410
LML	14	39.98	6.43	14	33.07	6.38	0.00208
RLL	14	37.46	5.16	14	29.03	8.71	0.00296
LLL	14	36.15	3.40	14	30.43	6.51	0.00003

Table 7. Median lobar tortuosity per case within generations 2–6.

	Normal			Idiopathic pulmonary fibrosis			
Lobe	n	Median	IQR	n	Median	IQR	p-value
RUL	14	1.030	0.006	14	1.032	0.007	0.13700
LUL	14	1.028	0.007	14	1.032	0.005	0.00915
RML	14	1.025	0.011	14	1.031	0.009	0.15000
LML	14	1.025	0.008	14	1.035	0.011	0.00674
RLL	14	1.026	0.004	14	1.037	0.012	0.00065
LLL	14	1.026	0.004	14	1.032	0.005	0.00208

Table 8. Median lobar intertapering per case within generations 7 + .

	Normal			Idiopathic pulmonary fibrosis			
Lobe	n	Median	IQR	n	Median	IQR	p-value
RUL	6	28.36	3.91	12	25.72	7.71	0.43700
LUL	4	32.93	6.79	5	21.09	18.95	0.41300
RLL	14	37.50	10.39	14	25.87	8.04	0.00042
LLL	12	33.95	6.61	14	27.36	8.72	0.00448

Table 9. Median lobar tortuosity per case within generations 7 + .

	Normal			Idiopathic pulmonary fibrosis			
Lobe	n	Median	IQR	n	Median	IQR	p-value
RUL	6	1.024	0.013	12	1.036	0.012	0.02450
LUL	4	1.026	0.010	5	1.052	0.045	0.19000
RLL	14	1.020	0.005	14	1.033	0.015	<0.00001
LLL	12	1.023	0.012	14	1.034	0.012	0.02340

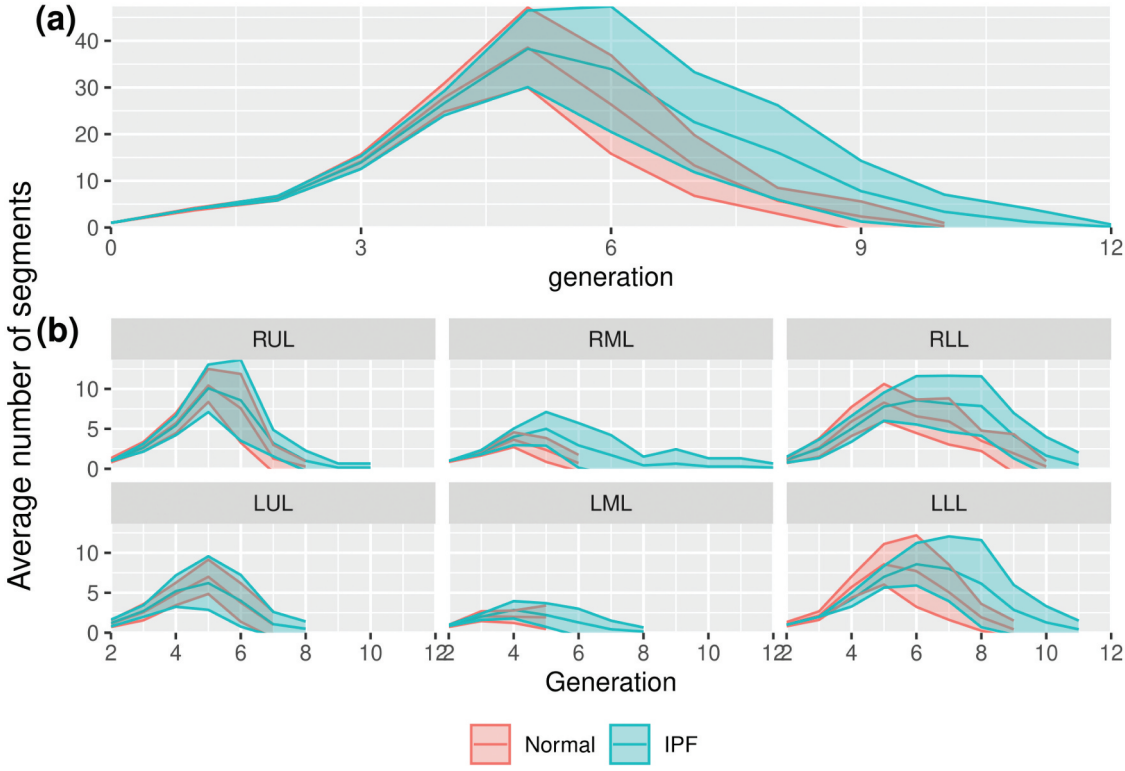

Figure 5. Line plot showing mean number of segments with shaded standard deviation per generation across all patients, differentiating between normal healthy participants and idiopathic pulmonary fibrosis (IPF) patients for each lobe. Lobar generation 2 is the first generation of that lobe. RUL=right upper lobe, LUL=left upper lobe, RML=right middle lobe, LML=left middle lobe, RLL=right lower lobe, LLL=left lower lobe.

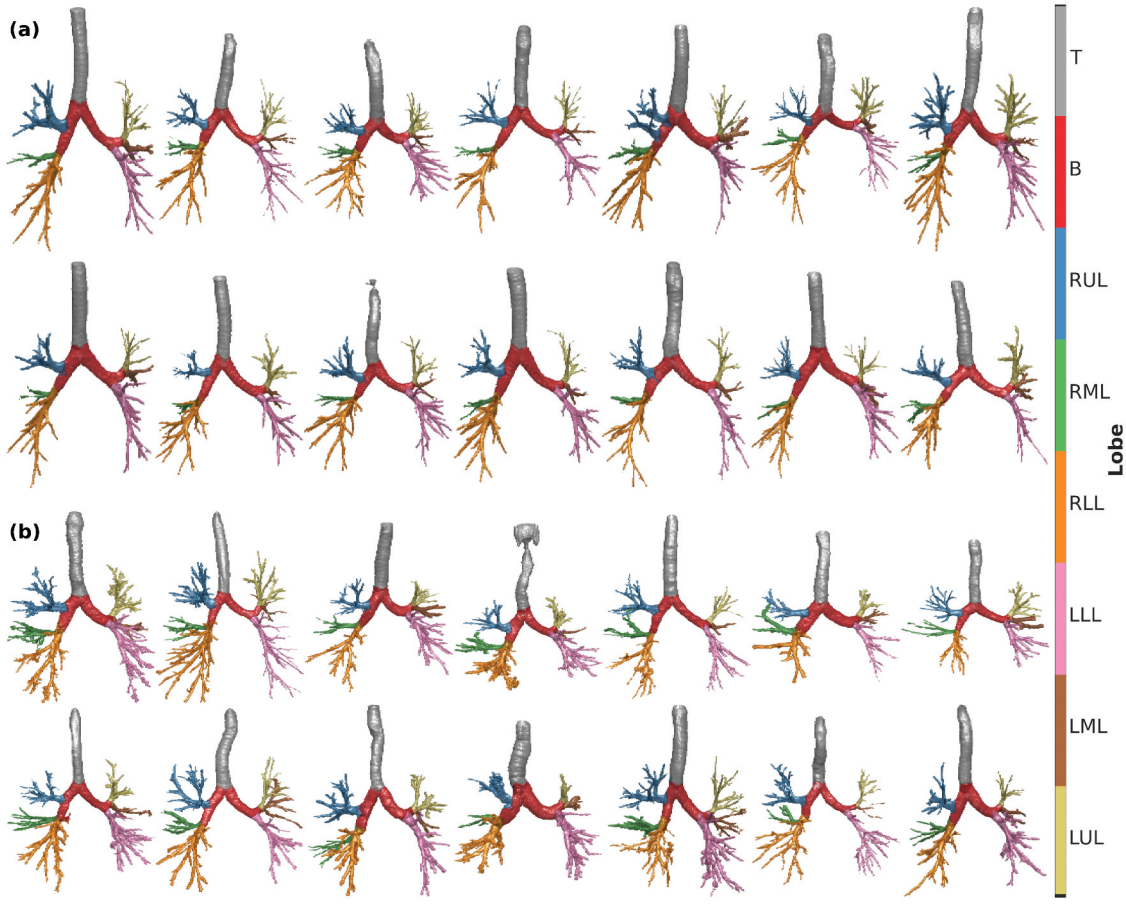

Figure 6. Visual airway segmentation results for all (a) normal healthy participants (b) idiopathic pulmonary fibrosis patients. Colour indicates lobar classification with colour bar shown. RUL=right upper lobe, LUL=left upper lobe, RML=right middle lobe, LML=left middle lobe, RLL=right lower lobe, LLL=left lower lobe.

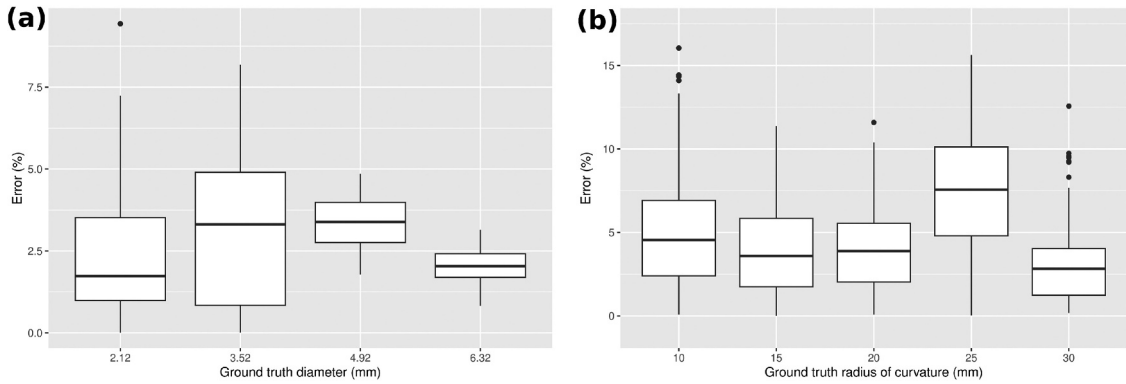

Figure 7. Box plots showing diameter measurement error on two sets of phantom airways. (a) Straight phantoms of fixed diameter. (b) Curved phantoms of fixed 2.12 mm diameter.

(139.50–191.25) respectively. Failure in the pipeline only occurred at the lobe classification phase. All lobe classifications were visually checked and manually corrected if necessary before further analysis. Two IPF and two normal cases had LUL airways mislabelled as lingular airways. One IPF case had RLL airways mislabelled as RUL airways. One healthy volunteer exhibited an anatomical variant whereby two RUL branches originated from the right main bronchus and these were mislabelled. Airway segmentation results and final lobe classifications are shown in Figure 6. Each case took 10–20 min to process in MATLAB on a 3 GHz Intel-i7 9th gen. processor with 16GB memory workstation. The only manual involvement was of very brief lobe classification corrections to six anomalous cases.

3.1. Phantom analysis

Results of measurements on the phantom airways are shown in Figure 7. It was found that measurements of the straight phantoms down to 2.12 mm diameter had a median error of less than 5%. This error appeared to increase for curved phantoms, but nevertheless only showed a maximum median error of 7.6%.

3.2. Airway Level Quantitative Analysis

When the intertapering gradient was evaluated at the airway level across the normal generation range, a significant reduction ($p \leq 0.004$) in intertapering gradient was found in IPF

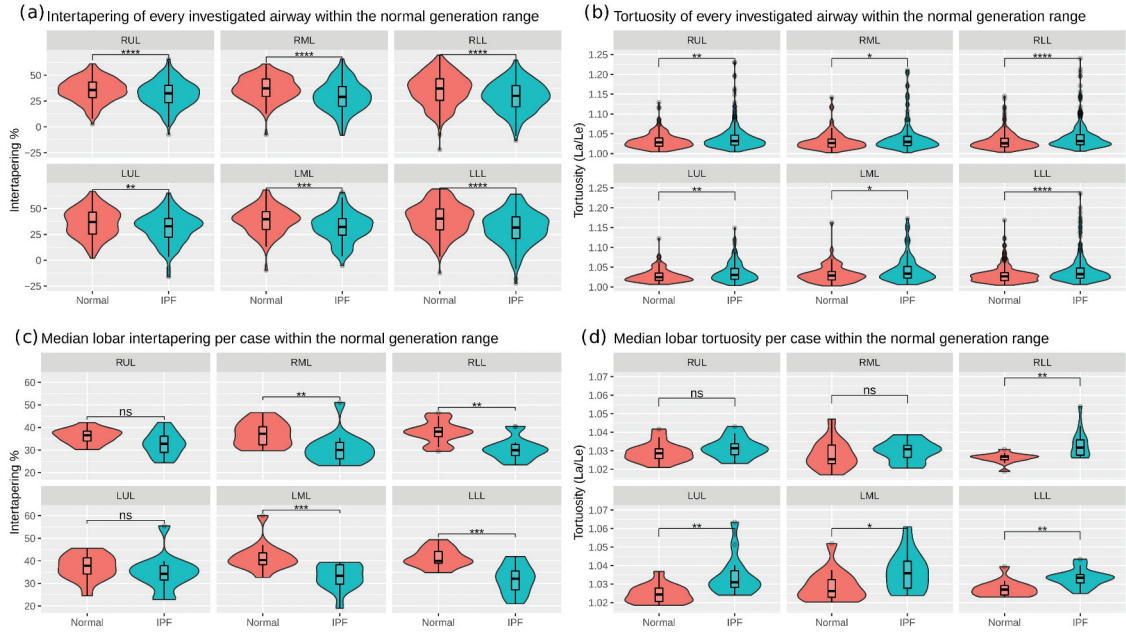

Figure 8. Violin-box plots comparing normal healthy participants and idiopathic pulmonary fibrosis (IPF) patients. The level of significance for the Mann-Whitney U tests for each lobe is shown above the respective plot. (a) and (b) considers every airway segment from every subject in each group. (c) and (d) considers the median lobar values on a per patient basis within the normal generational range. RUL=right upper lobe, LUL=left upper lobe, RML=right middle lobe, LML=left middle lobe, RLL=right lower lobe, LLL=left lower lobe. ns, not significant, *$p < 0.05$, **$p < 0.01$, ***$p < 0.001$, ****$p < 0.0001$ in Mann-Whitney U comparison tests.

patients compared to healthy volunteers. Airways from patients with IPF were shown to taper less than airways in healthy volunteers (Table 2, Figure 8(a)). Airway tortuosity was significantly greater ($p \leq 0.034$) in IPF patients than healthy volunteers (Table 3, Figure 8(b)). Differences were most marked within the lower lobes, in keeping with the typical distribution of IPF airway abnormalities.

For airway changes examined at the patient level, significant reductions in intertapering were seen in IPF patients in the middle ($p \leq 0.004$) and lower lobes ($p \leq 0.002$) compared to healthy volunteers (Table 4, Figure 8(c)). Airway tortuosity was similarly significantly increased in the LML ($p \leq 0.035$) and both lower lobes ($p \leq 0.002$) (Table 5, Figure 8(d)). The results reflect the lower zone distribution of disease typically seen in IPF patients.

3.3. Patient level quantitative analysis

When airway metrics were examined at a patient level for generations 2–6, the segmental intertapering value was significantly reduced ($p \leq 0.044$) in IPF patients in all lobes. Differences were most marked within the lower lobes ($p \leq 0.003$) (Table 6, Figure 9(a)). Segmental airway tortuosity was significantly increased in left-sided lung lobes ($p \leq 0.009$) and the RLL ($p \leq 0.001$)(Table 7, Figure 9(b)). Mean diameter per generation per lobe is visualised for each case in Figure 10. This gives an intuitive comparison of how airway diameter changes across the 2nd to 6th generation between the two groups. Airway diameters are generally larger across all generations (with a shallower gradient change: intertapering) in IPF patients when compared to normal subjects.

Airways at generations 7 and beyond were not routinely seen in the middle lobes. Accordingly, airway metrics for generation 7 and beyond were only examined in the upper and lower lobes. Significant differences in segmental intertapering ($p \leq 0.004$) (Table 8, Figure 9(c)) and segmental airway tortuosity ($p \leq 0.023$)(Table 9, Figure 9(d)) were seen in the lower lobes between IPF patients and healthy volunteers.

Segmentations and AirQuant graphs in two sex and age-matched individuals (one IPF and one control) are visualised in Figure 11. This figure demonstrates the utility of the reduced representation of airways as an AirQuant generated graph. This depiction gives a more precise visualisation in 2D of the number of segments visible per lobe and per airway generation as well as the mean diameter of individual segments. The visualisation allows an intuitive sense of extent and severity of traction bronchiectasis on a lobar basis.

4. Discussion

Our results highlight the potential for CT-based morphological airway measurements to identify differences in disease extent and severity of traction bronchiectasis in patients with IPF. To date airway damage in IPF has been thought to be a primarily distal airway phenomenon. Our proof of concept study, despite having a relatively small sample size of 14 IPF cases and healthy controls have supported this by showing that the largest distinction in intertapering and tortuosity between healthy volunteers and IPF patients was seen in the most distal airway generations, beyond the seventh generation. Yet the identification of a reduction in airway intertapering and increase in tortuosity in proximal airway branches (in the 2nd-6th generations) suggests that subtle damage does affect the central airways in IPF, a finding previously under-recognised. The regional analysis achieved by AirQuant can provide valuable morphological insights when applied across sub-regions of the airway

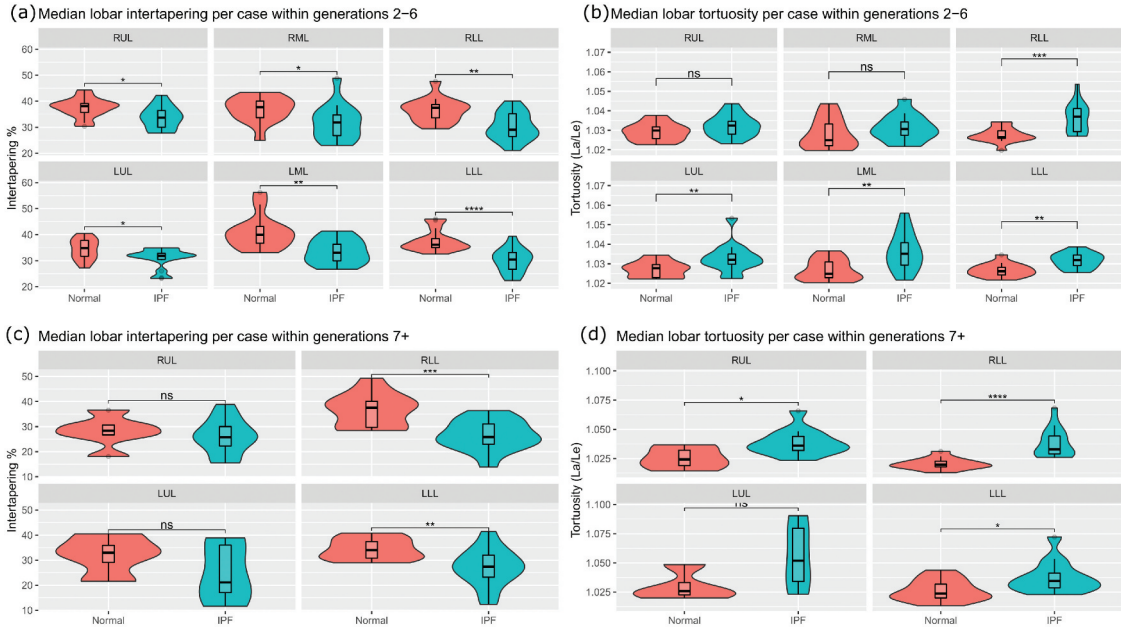

Figure 9. Violin-box plots comparing airways on a per patient basis in normal healthy participants and idiopathic pulmonary fibrosis (IPF) patients. The level of significance of the Mann-Whitney U test for each lobe is shown above the respective plot. (a) and (b) consider airway segments between generations two and six. (c) and (d) only consider airway segments from generation 7 onwards. RUL=right upper lobe, LUL=left upper lobe, RML=right middle lobe, LML=left middle lobe, RLL=right lower lobe, LLL=left lower lobe. ns, not significant, *$p < 0.05$, **$p < 0.01$, ***$p < 0.001$, ****$p < 0.0001$ in Mann-Whitney U comparison tests.

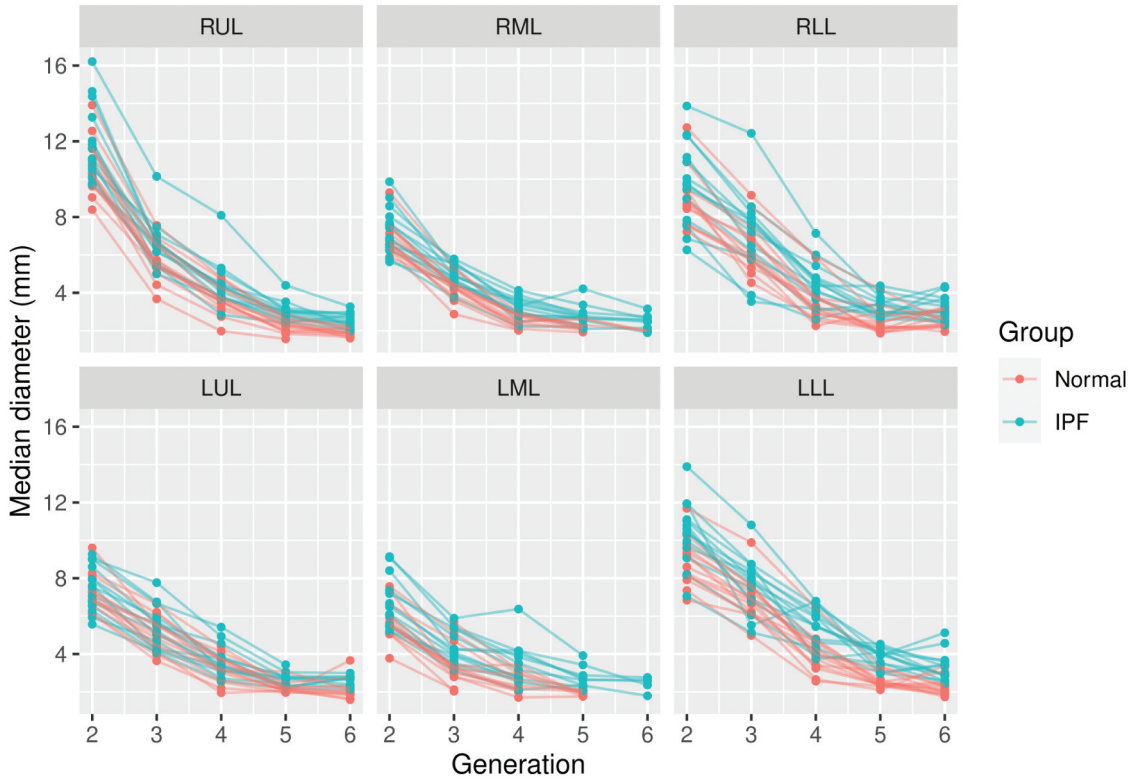

Figure 10. Median diameter per generation per lobe of every case. This is a graphical visualisation of diameter change (intertapering) across the 2–6 generation range for normal healthy individuals and idiopathic pulmonary fibrosis (IPF) patients. Joined points signify the same case. RUL=right upper lobe, LUL=left upper lobe, RML=right middle lobe, LML=left middle lobe, RLL=right lower lobe, LLL=left lower lobe.

tree. This is an advantage over pulmonary function tests which provide global measures of lung damage, and many quantitative CT algorithms which only estimate whole lung disease extents.

Our findings are comparable to previous analyses of intertapering gradients of proximal airways in patients with idiopathic bronchiectasis and healthy controls Kuo et al. (2020). Our results diverged from Kuo et al. (2020) when more distal airways were evaluated, reflecting the ability of our 2D-UNet segmentation to identify larger numbers of more distal airway branches. A key advantage of AirQuant lies in its automation, which allows hundreds of airways in a single patient, captured by modern segmentation methods, to be comprehensively analysed. The automation built into AirQuant is crucial for the feasibility of clinical evaluation of large patient cohorts.

The concept that traction bronchiectasis scored visually on CT imaging could be a prognostic variable in IPF patients was first described almost 15 years ago Sumikawa et al. (2008); Edey et al. (2011). More recently, change in visual traction bronchiectasis scores has been shown to identify disease progression on longitudinal IPF imaging Jacob et al. (2020). The challenges associated with employing visual traction bronchiectasis estimation however are many. These include the time consuming nature of visual analysis, the requirement for expert reads of the images, where experts are typically in short supply, are expensive to employ and are prone to interobserver variation Jacob et al. (2016).

The motivation behind the current study was the idea that automating airway tapering assessments would alleviate some of the challenges associated with visual CT estimation of traction bronchiectasis by providing an objective, rapid and sensitive measure of lung disease severity in IPF. Accordingly, we chose to use automated segmentation methods, specifically to demonstrate that meaningful measures can be derived using AirQuant without recourse to labour-intensive manual labelling of the extensive airway network.

AirQuant was successful in examining every case, but relies on a good lumen segmentation. Whilst our pipeline can be implemented following any airway segmentation method, missed airways in a segmentation can affect the cross-sectional comparison between subjects. It is expected that the number of airways almost exponentially increase across successive airway generations. In this study, the mean number of airways followed this trend to the 5th lobar generation globally in the lungs, and to the 6th generation in diseased lower lobes. In healthy controls, as the airways are inherently smaller and thinner, we see fewer segments at each generation. Airways become larger and easier to identify with disease. It is therefore to be expected that when comparing healthy lungs to diseased lungs, fewer airway segments might be identified in healthy cases rather than those with disease.

Airway lumen segmentation is heavily influenced by CT acquisition and reconstruction parameters. A larger x-ray focal point, larger detector size, larger field of view, larger slice spacing and reduced dose can result in reduced

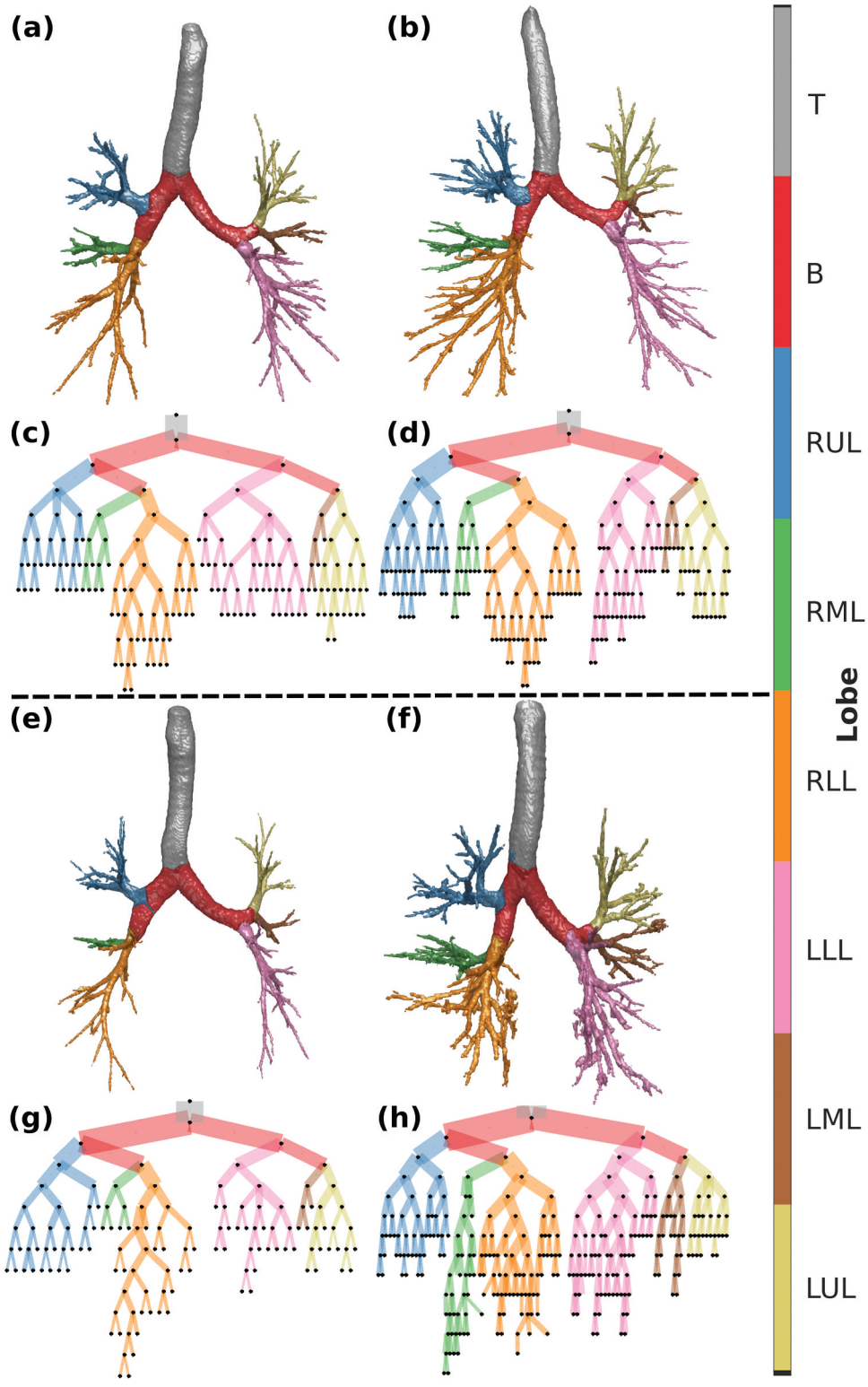

Figure 11. Two pairs of age and sex matched cases between the normal healthy group (a,e) and idiopathic pulmonary fibrosis group (b,f). Cases (a) and (b) are a 55 and 56 year old females with forced vital capacity (FVC) of 100 and 102% respectively. Cases (e) and (f) are a 52 and 51 year old males with FVC of 96 and 56 % respectively. (a,b,e,f) shows airway segmentation and lobar classification by colour with colour bar shown. (c,d,g,h) shows corresponding respective graph network visualisation of airways derived by AirQuant where each airway segment is represented by an edge with thickness proportionate to mean airway lumen diameter. Lobar classification also shown by colour. RUL=right upper lobe, LUL=left upper lobe, RML=right middle lobe, LML=left middle lobe, RLL=right lower lobe, LLL=left lower lobe.

resolution and therefore fewer airways identified. Similarly, the presence of contrast agents and particular certain reconstruction kernels can affect CT density and therefore airway measurement. A limitation of this analysis was that these parameters could not be controlled retrospectively. Nevertheless, the airway measurement method described in this paper was validated on gold-standard 3D printed phantoms down to 2.12 mm diameter. The majority of AirQuant

airway measurements were found to be accurate within 5% of the ground truth diameter which is an acceptable level of accuracy when translated to clinical CT imaging.

Our airway lobe classification algorithm can be affected by anatomical variants although these are relatively uncommon Gu et al. (2012). In mitigation of this, the lobe classification of individual airways can be easily retrospectively corrected in our pipeline. As future work we aim to improve the robustness with which our lobar classification system deals with anatomical variants which will likely be present in very large data sets ($>>1000$). Our existing lobe classification algorithm can help develop training data for methods more suitable to analysing large-scale datasets such as learning graphical neural networks.

In the more distal airway generations, an AirQuant segmental branch may in fact consist of multiple anatomical segments. This may occur if sibling branch points are not identified in the segmentation and therefore not acknowledged as bifurcations. Though unlikely in the central airways, it can affect metrics in distal generations. With the improvement of modern segmentation methods, this issue will become less of a constraint.

Efforts have been made to make the centreline extraction and graph conversion stage robust to loops. However, when coming across branches that cause loops, it is difficult to determine which graph edge is the valid airway branch and which is the anomaly. It is likely that the wrong graph edge may have been removed in some cases, as it is not trivial to identify the anomaly in an automated way. For future work, it will be important to validate the clinical impact of our measurements on larger IPF datasets.

In conclusion, we have demonstrated that the airway inter-tapering gradient is reduced and airway tortuosity enhanced in IPF patients compared to healthy participants. The findings were accentuated in the lower lobes which is consistent with the typical distribution of traction bronchiectasis in IPF. Our pilot analyses suggest that automated airway analyses show great promise for the assessment of disease severity and extent, both in IPF trials and for clinical care.

Note

1. https://github.com/tomdoel/pulmonarytoolkit

Acknowledgements

This research was funded in whole or in part by the Wellcome Trust (209553/Z/17/Z). For the purpose of open access, the author has applied a CC-BY public copyright licence to any author accepted manuscript version arising from this submission. This project was also supported by CMIC Platform EPSRC (EP/M020533/1) and the NIHR UCLH Biomedical Research Centre, UK. JJ and WKC were supported by Rosetrees Award JS15/M851. JJ and AP were supported by a Cystic Fibrosis Trust Venture and Innovation Award 059. AP was supported by i4health EPSRC (EP/S021930/1).

Disclosure statement

JJ reports fees from Boehringer Ingelheim, Roche, NHSX, Takeda, Gilead, Microsoft Research and GlaxoSmithKline unrelated to the submitted work. JJ reports UK patent application numbers 2,113,765.8 and GB2211487.0 unrelated to the submitted work.

Funding

The work was supported by the Cystic Fibrosis Trust; EPSRC Centre for Doctoral Training in Medical Imaging; Wellcome Trust.

Notes on contributors

Ashkan Pakzad graduated with an MSci in Medical Physics (2017) and PhD in Medical Imaging (2023) from University College London. His research interests are in machine learning and computer vision for medical image analysis with a focus on translation and practical application. His PhD was in quantifying airway morphology in chronic lung disease.

Wing Keung Cheung received the B.Sc. and M.Phil. degrees in physics from the Hong Kong University of Science and Technology, in 2003 and 2005, respectively, and the Ph.D. degree in bioengineering from Imperial College London, in 2016. He was a Postdoctoral Research Assistant with the School of Engineering and Materials Science, Queen Mary University of London. He was a Research Fellow with the Centre of Medical Image Computing, University College London. His research interests include deep learning, machine learning, artificial intelligence, medical image computing, ultrasound elastography and biomechanics.

Dr. Coline van Moorsel is Head ILD Research and R&D Pulmonology at St Antonius ILD center of excellence, Nieuwegein. Furthermore, she is assistant professor at University Medical Center Utrecht. She received her MSc degree in Biology with honors from Leiden University and after her PhD and postdoc on genotype-phenotype associations, she joined St Antonius Hospital to study the pathobiology of Interstitial Lung Disease (ILD). The focus of her research, and the PhD students she supervises, is on the genetic factors that determine development and evolution of ILD. She chaired the ERS taskforce on familial pulmonary fibrosis and is currently chair of the NIH ClinGen ILD gene curation expert panel.

Kin Quan is an analyst in NHS England. A mathematician by background, he completed his PhD in medical imaging at University College London in 2019 on quantifying airway dilatation and tapering. His recent work and interests include data linkage, artificial data and data wrangling or munging of health records in the NHS. GitHub profile: https://github.com/quan14

Dr. Nesrin Mogulkoc is currently a Professor of Chest Medicine at Ege University Hospital, Bornova, Izmir, Turkiye. Her main interests are interstitial lung diseases, sarcoidosis, and pulmonary hypertension. She runs a regional referral center for PAH and ILD at Ege University Hospital. She has an active role for ILD and PAH in national and international organizations. She was on the organizing committee of the World Conference of WASOG which was held in Izmir, Turkey in October 2014. She is on the steering committees of the Empire registry for IPF and the Turkish national registry for UIP. She gained experience in the Heart and Lung Transplantation Unit and the North West Lung Research Centre, both being at the University Hospital of South Manchester, UK. At that time, she was working under the guidance of Dr. J. Egan, the lead transplant and ILD chest physician in the department.

Dr. Bartholmai is an innovator and leader in Thoracic Radiology, Radiology Informatics and Quantitative Imaging of thoracic disease. He is the former chair of the Division of Radiology Informatics at Mayo Clinic and is active in clinical practice, research, education and innovation.

Wouter van Es is a cardiothoracic radiologist at the St. Antonius Hospital in Nieuwegein, The Netherlands. He obtained his Medical Degree at Utrecht University in 1990. He finished his Radiology training in The University Medical Center Utrecht in 1996. He earned his doctorate at the University in Utrecht in 1997 (thesis: "MR Imaging of the brachial plexus"). Since 1997 he works in St. Antonius Hospital in Nieuwegein as a staff member and is specialised in the radiology of interstitial lung diseases. He participates in the Expertise Center for Interstitial Lung Diseases in his hospital and is

active in the radiology of interstitial lung disease as well clinically as scientifically.

Dr Alper Ezircan is a Medical Doctor and PhD student at Ege University Hospital, Bornova, Izmir, Turkiye.

Frouke Van Beek is a pulmonologist (MD) working at the ILD Center of Excellence in St. Antonius Hospital. Dr Van Beek trained as a physician at VU University Amsterdam before specialising in 2007.

Marcel Veltkamp is a pulmonologist working at the ILD Center of Excellence of the St. Antonius Hospital Nieuwegein which is a national expert centre for Interstitial Lung Diseases (ILD) and Sarcoidosis in the Netherlands. He is the current secretary of the European Respiratory Society (ERS) Assembly on Sarcoidosis (12.03), board member of the Netherlands Respiratory Society (NRS) and a member of the WASOG executive Committee. He is also involved in the Foundation for Sarcoidosis Clinical Studies Network. His research interests include sarcoidosis (aetiology, different treatment strategies, biomarkers, small fibre neuropathy), pulmonary fibrosis (treatment, genetics) and Pulmonary Alveolar Proteinosis.

Dr Ronal Karwoski (retired) was Biomedical Imaging Software Development Lead at the Biomedical Imaging Resource at the Mayo Clinic, Rochester, Minnesota.

Dr. Tobias Peikert is a pulmonologist and critical care specialist currently working at the Mayo Clinic in Minnesota. Throughout his career, Dr. Peikert has been heavily involved in research for a number of diseases, including mesothelioma. He has helped author numerous medical studies around the rare cancer, investigating new treatments for all types of cancer, surgical reduction for epithelioid mesothelioma, particular genes that have been associated with mesothelioma, as well as investigating new modes of immunotherapy.

Dr. Ryan Clay is a pulmonary and critical care specialist who practises at Kaiser Permanente in Oregon where he is director of their pulmonary function lab. He obtained his undergraduate degree from New York University and his medical degree from the University of Minnesota. He completed his pulmonary and critical care fellowship at the Mayo Clinic in Minnesota.

Dr. Finbar Foley is a pulmonary and critical care physician and Assistant Professor at the Yale School of Medicine. During his fellowship at the Mayo Clinic in Rochester, he worked as part of a biomedical imaging team applying machine learning to CT imaging of normal lung parenchyma, diffuse lung diseases, and lung nodules. His current clinical interests include the care of patients with neuromuscular disease impacting respiration and lung cancer screening. He is also invested in medical education at the resident and fellow level.

Cassandra Braun is a pulmonary and critical care physician at Mayo Clinic, Rochester, MN. Dr. Braun serves as the current program director for the pulmonary disease fellowship. Her areas of interest include fellow eduction, critical care, interstitial lung disease, workup of lung nodules/mass, and management of pleural disease.

Professor Dr. Recep Savaş has been working as a Thoracic Radiologist at Ege University Faculty of Medicine, Department of Radiology since 1995. His main areas of interest are lung malignancies, interstitial lung diseases and PET/CT imaging. He is currently the president of the Turkish Thoracic Radiology Association. At the same time, as a paediatric radiologist, he continues his duty as the head of the Pediatric Radiology Department at the same university. He worked as a consultant radiologist in foreign centres besides the university for many years.

Dr Carole Sudre is a Lecturer in Data Science for Health at the University College London, United Kingdom. With a background in biomedical engineering and applied mathematics from Ecole Polytechnique (France) and ETH Zurich (Switzerland), her research focuses on the development of methods for automated biomarkers extraction from medical imaging and their application on large population data. She has a particular interest in the modelling of uncertainty, validation methods and the identification of very subtle markers of interest.

Dr Tom Doel is a software consultant based in the United Kingdom. He previously held research positions at UCL and the University of Oxford, and software development positions at Barco Medical Imaging Systems, formerly Voxar. His research interests include pulmonary image analysis, computational modelling of the respiratory system, and software for pre-operative surgical planning and image guided surgery. His doctorate at the University of Oxford involved developing novel methods for assessing pulmonary disease using xenon MRI and multi-modal image analysis. He holds masters degrees from the University of Bath and the University of Edinburgh.

Daniel C. Alexander is an Director of the Centre for Medical Image Computing (CMIC: https://www.ucl.ac.uk/medical-image-computing/ucl-centre-medical-image-computing-cmic) and deputy head of the Computer Science Department at UCL. I lead the Microstructure Imaging Group and the Progression of Neurodegenerative Diseases initiative. I am theme lead for the UCLH Biomedical Research Centre Healthcare Engineering and Imaging theme. My core expertise is in computer science, computational modelling, machine learning, and imaging science. My first degree was a BA in Mathematics from Oxford completing in 1993. I then studied for MSc and PhD in Computer Science at UCL, completing in 1997. After a post-doc at the University of Pennsylvania, I returned to UCL as a lecturer in 2000 and I have been Professor of Imaging Science since 2009.

Dr. Wijeratne is a Lecturer / Assistant Professor in Computer Science and AI at the University of Sussex. He has an education in physics and postdoctoral training in engineering and computer science. From 2019-2022 he held a UK Research Research and Innovation (UKRI) Medical Research Council (MRC) Skills Development Fellowship, during which he developed longitudinal data-driven probabilistic models of disease progression. His current focus is on generalising these models to other spatiotemporal processes, such as neurodevelopment.

David Hawkes is Emeritus Professor of Medical Physics and Biomedical Engineering at UCL, London. He is a physicist with 49 years' experience in medical imaging research, working closely with healthcare providers and industry to translate novel imaging science to the clinic. His main research interests have encompassed multi-modal modelling, multi-scale interpretation and image registration applied to cancer imaging, lung imaging, cardiovascular imaging and image directed interventions. He was appointed Professor of Computational Imaging Sciences at KCL in 1998 , moving to UCL in 2005 where he founded and directed the UCL Centre for Medical Image Computing. He was appointed interim director of the Wellcome EPSRC Centre for Interventional and Surgical Sciences (WEISS) from 2018 to 2019.

Yipeng Hu is an academic staff at the Department of Medical Physics and Biomedical Engineering, University College London. His current research interest is applying machine learning and computational algorithms in medical image analysis and image-guided intervention.

John Hurst is Professor of Respiratory Medicine at University College London, and a clinical academic with a particular research interest in chronic airways diseases.

Joseph Jacob runs the Satsuma Lab at the Centre for Medical Image Computing, University College London which centers on computational image analysis of the lungs and heart on CT imaging. He was awarded an eight-year Wellcome Trust Career Development Fellowship in 2024.

ORCID

JR. Hurst http://orcid.org/0000-0002-7246-6040

References

Bhalla M, Turcios N, Aponte V, Jenkins M, Leitman BS, McCauley DI, Naidich DP. 1991. Cystic fibrosis: scoring system with thin-section CT. Radiology. 179(3):783–788. doi: 10.1148/radiology.179.3.2027992.

Burrowes K, Doel T, Kim M, Vargas C, Roca J, Grau V, Kay D. 2017. A combined image-modelling approach assessing the impact of hyperinflation due to emphysema on regional ventilation–perfusion matching. Comput Meth Biomech Biomed Eng Imaging Vis. 5(2):110–126. doi: 10.1080/21681163.2015.1023358.

Chollet F. 2015. Keras. https://keras.io/getting_started/faq/#how-should-i-cite-keras.

Collard HR, Bradford WZ, Cottin V, Flaherty KR, King TE, Koch GG, Kolb M, Martinez FJ, Montgomery B, Raghu G, et al. 2015. A new era in idiopathic pulmonary fibrosis: considerations for future clinical trials. Eur Respir J. 46(1):243–249. doi:10.1183/09031936.00200614.

Dave MH, Gerber A, Bailey M, Gysin C, Hoeve H, Hammer J, Nicolai T, Weiss M. 2014. The prevalence of tracheal bronchus in pediatric patients undergoing rigid bronchoscopy. J Bronchology Interv Pulmonol. 21 (1):26–31. doi: 10.1097/LBR.0000000000000029.

Diaz AA, Young TP, Maselli DJ, Martinez CH, Gill R, Nardelli P, Wang W, Kinney GL, Hokanson JE, Washko GR, et al. 2017. Quantitative CT measures of bronchiectasis in smokers. Chest. 151(6):1255–1262. doi:10.1016/j.chest.2016.11.024.

Dice LR. 1945. Measures of the amount of ecologic association between species. Ecology. 26(3):297–302. doi: 10.2307/1932409.

Doel T 2012. Developing clinical measures of lung function in COPD patients using medical imaging and computational modelling [PhD Thesis]. University of Oxford.

Doel T 2014. Pulmonary Toolkit. [software] commit: #09688a0; accessed 2021, May 19. Available from: https://github.com/tomdoel/pulmonarytoolkit.

Dunham-Snary KJ, Wu D, Sykes EA, Thakrar A, Parlow LRG, Mewburn JD, Parlow JL, Archer SL. 2017. Hypoxic pulmonary vasoconstriction: from molecular mechanisms to medicine. Chest. 151(1):181–192. doi: 10.1016/j.chest.2016.09.001.

Edey AJ, Devaraj AA, Barker RP, Nicholson AG, Wells AU, Hansell DM. 2011. Fibrotic idiopathic interstitial pneumonias: HRCT findings that predict mortality. Eur Radiol. 21(8):1586–1593. doi: 10.1007/s00330-011-2098-2.

Fitzgibbon AW, Pilu M, Fisher RB 1996. Direct least squares fitting of ellipses. In: Proceedings of 13th International Conference on Pattern Recognition, Vienna, Austria; vol. 1; Aug. p. 253–257 vol.1.

Goodfellow I, Bengio Y, Courville A 2016. Deep Learning. MIT Press. Available from: https://www.deeplearningbook.org/ .

Gu S, Wang Z, Siegfried JM, Wilson D, Bigbee WL, Pu J. 2012. Automated lobe-based airway labeling. Int J Biomed Imaging. 2012:1–9. doi: 10.1155/2012/382806.

Hansell DM, Bankier AA, MacMahon H, McLoud TC, Müller NL, Remy J. 2008. Fleischner Society: glossary of terms for thoracic imaging. Radiology. 246 (3):697–722. doi: 10.1148/radiol.2462070712.

Hansell D, Lynch D, McAdams H, Bankier A. 2009. Imaging of diseases of the chest E-Book. United States: Elsevier Health Sciences.

Hutchinson J, Fogarty A, Hubbard R, McKeever T. 2015. Global incidence and mortality of idiopathic pulmonary fibrosis: a systematic review. Eur Respir J. 46(3):795–806. doi: 10.1183/09031936.00185114.

Jacob J, Aksman L, Mogulkoc N, Procter AJ, Gholipour B, Cross G, Barnett J, Brereton CJ, Jones MG, Moorsel C, et al. 2020. Serial CT analysis in idiopathic pulmonary fibrosis: comparison of visual features that determine patient outcome. Thorax. 75(8):648–654. doi:10.1136/thoraxjnl-2019-213865.

Jacob J, Bartholmai BJ, Rajagopalan S, Kokosi M, Nair A, Karwoski R, Raghunath SM, Walsh SLF, Wells AU, Hansell DM. 2016. Automated quantitative computed tomography versus visual computed tomography scoring in idiopathic pulmonary fibrosis: validation against pulmonary function. J Thorac Imaging. 31(5):304–311. doi: 10.1097/RTI.0000000000000220.

Johannson KA, Ley B, Collard HR. 2015. Models of disease behavior in idiopathic pulmonary fibrosis. BMC Med. 13(1):165. doi: 10.1186/s12916-015-0403-7.

Kim JS, Müller NL, Park CS, Lynch DA, Newman LS, Grenier P, Herold CJ. 1997. Bronchoarterial ratio on thin section CT: comparison between high altitude and sea level. J Comput Assist Tomogr. 21(2):306–311. doi: 10.1097/00004728-199703000-00028.

Kingma DP, Ba J. 2014. Adam: a method for stochastic optimization. arXiv. doi: 10.48550/arXiv.1412.6980.

Kiraly AP, Reinhardt JM, Hoffman EA, McLennan G, Higgins WE. 2005. Virtual bronchoscopy for quantitative airway analysis. In: Amini A, and Manduca A, editors. Medical imaging 2005: physiology, function, and structure from medical images. Vol. 5746. United States: Apr. International Society for Optics and Photonics; p. 369.

Kollmannsberger P, Kerschnitzki M, Repp F, Wagermaier W, Weinkamer R, Fratzl P. 2017. The small world of osteocytes: connectomics of the lacuno-canalicular network in bone. New J Phys. 19(7):073019. doi: 10.1088/1367-2630/aa764b.

Kuo W, Perez-Rovira A, Tiddens H, de Bruijne M. 2020. Airway tapering: an objective image biomarker for bronchiectasis. Eur Radiol. 30 (5):2703–2711. doi: 10.1007/s00330-019-06606-w.

Lo P, Van Ginneken B, Reinhardt JM, Yavarna T, De Jong PA, Irving B, Fetita C, Ortner M, Pinho R, Sijbers J, et al. 2012. Extraction of airways from CT (EXACT'09). IEEE Trans Med Imaging. 31(11):2093–2107. doi:10.1109/TMI.2012.2209674.

Martín A, Ashish A, Paul B, Eugene B, Zhifeng C, Craig C, Greg S, Corrado AD, Dean J, Matthieu D, et al. 2015. TensorFlow: large-scale machine learning on heterogeneous systems. Available from: http://tensorflow.org/.

Matsuoka S, Uchiyama K, Shima H, Ueno N, Oish S, Nojiri Y. 2003. Bronchoarterial ratio and bronchial wall thickness on high-resolution CT in asymptomatic subjects: correlation with age and smoking. Am J Roentgenol. 180(2):513–518. doi: 10.2214/ajr.180.2.1800513.

Odry BL, Kiraly AP, Novak CL, Naidich DP, Lerallut JF. 2006. Automated airway evaluation system for multi-slice computed tomography using airway lumen diameter, airway wall thickness and broncho-arterial ratio. In: Manduca A Amini A, editors Medical imaging 2006: physiology, function, and structure from medical images. San Diego, CA: Mar; p. 61430Q.

Palágyi K, Tschirren J, Hoffman EA, Sonka M. 2006. Quantitative analysis of pulmonary airway tree structures. Comput Biol Med. 36(9):974–996. doi: 10.1016/j.compbiomed.2005.05.004.

Petersen J, Nielsen M, Lo P, Nordenmark LH, Pedersen JH, Wille MMW, Dirksen A, de Bruijne M. 2014. Optimal surface segmentation using flow lines to quantify airway abnormalities in chronic obstructive pulmonary disease. Med Image Anal. 18(3):531–541. doi: 10.1016/j.media.2014.02.004.

Quan K, Shipley RJ, Tanno R, McPhillips G, Vavourakis V, Edwards D, Jacob J, Hurst JR, Hawkes DJ. 2018. Tapering analysis of airways with bronchiectasis. In: editors, Angelini E, and Landman B. Medical imaging 2018: image processing, Mar. SPIE, Vol. 10574. United States: SPIE. p. 87

Raghu G, Remy-Jardin M, Myers JL, Richeldi L, Ryerson CJ, Lederer DJ, Behr J, Cottin V, Danoff SK, Morell F, et al. 2018. Diagnosis of idiopathic pulmonary fibrosis. An official ATS/ERS/JRS/ALAT clinical practice guideline. Am J Respir Crit Care Med. 198(5):e44–e68. doi:10.1164/rccm.201807-1255ST.

Spencer LG, Loughenbury M, Chaudhuri N, Spiteri M, Parfrey H. 2021. Idiopathic pulmonary fibrosis in the UK: analysis of the British thoracic society electronic registry between 2013 and 2019. ERJ Open Res. 7 (1):00187–2020. doi: 10.1183/23120541.00187-2020.

Sumikawa H, Johkoh T, Colby TV, Ichikado K, Suga M, Taniguchi H, Kondoh Y, Ogura T, Arakawa H, Fujimoto K, et al. 2008. Computed tomography findings in pathological usual interstitial pneumonia. Am J Respir Crit Care Med. 177(4):433–439. doi:10.1164/rccm.200611-1696OC.

Weibel ER, Gomez DM. 1962. Architecture of the human lung: use of quantitative methods establishes fundamental relations between size and number of lung structures. Science. 137(3530):577–585. doi: 10.1126/science.137.3530.577.

Weinheimer O, Achenbach T, Bletz C, Düber C, Kauczor HU, Heusse CP. 2008. About objective 3-D analysis of airway geometry in computerized tomography. IEEE Trans Med Imaging. 27(1):64–74. doi: 10.1109/TMI.2007.902798.

Weinheimer O, Wielpütz MO, Konietzke P, Heussel CP, Kauczor HU, Brochhausen C, Hollemann D, Savage D, Galbán CJ, Robinson TE. 2017. Fully automated lobe-based airway taper index calculation in a low dose MDCT CF study over 4 time-points. In: Styner M, and Angelini E, editors. Medical imaging 2017: image processing. Vol. 10133. United States: International Society for Optics and Photonics; SPIE; p. 101330U.

Westcott JL, Cole SR. 1986. Traction bronchiectasis in end-stage pulmonary fibrosis. Radiology. 161(3):665–669. doi: 10.1148/radiology.161.3.3786716.

Yu F, Koltun V. 2016. Multi-scale context aggregation by dilated convolutions. *arXiv*. doi:10.48550/arXiv.1511.07122.